

# HoloNeedle: Augmented Reality Guidance System for Needle Placement Investigating the Advantages of Three-Dimensional Needle Shape Reconstruction

Michael A. Lin<sup>1</sup>, Alexa F. Siu<sup>1</sup>, Jung Hwa Bae<sup>1</sup>, Mark R. Cutkosky<sup>1</sup>, and Bruce L. Daniel<sup>2</sup>

**Abstract**—Augmented reality (AR) systems have been proposed for medical needle procedures as alternatives to restore the physician's natural perspective and head motion parallax that are lost when using standard imaging methods. AR systems have assumed a rigid needle, but in practice, a needle can experience large deflections that can lead to significant errors. We combine an instrumented needle that measures bending deflections with optical tracking of the needle base for precision and an AR system to provide users with precise three-dimensional rendering of needle motion and deflection inside a body. In controlled tests, users guided a needle through 7 cm of tissue phantom to reach a 2-mm diameter target. We found that displaying needle shape allows users significantly reduce placement errors when compared to the rigid needle assumption. In addition, a new display technique called tip tangent extrapolation, based on the sensed needle endpoint and direction, allowed users to further reduce errors resulting in 26% less error when compared to a rigid needle assumption.

**Index Terms**—Virtual reality and interfaces, medical robots and systems, surgical robotics, steerable catheters/needles.

## I. INTRODUCTION

IMAGE-GUIDED medical needle procedures are commonly performed for clinical treatment. During these procedures, a needle is inserted into a specific area of the patient with the goal of either diagnosing, excising cancerous tissue, or placing radioactive seeds for treatment. Several imaging methods such as ultrasound (US), Computed-tomography (CT) or Magnetic Resonance Imaging (MRI) are used to guide the insertion. These traditional guidance methods have a number of issues:

Manuscript received February 24, 2018; accepted July 12, 2018. Date of publication August 6, 2018; date of current version August 17, 2018. This letter was recommended for publication by Associate Editor J. Kim and Editor K. Masamune upon evaluation of the reviewers' comments. This work was supported in part by the NSF award CHS-1615891, in part by NSF-GRFP award DGE-114747, in part by the Stanford SoE Fellowship, and in part by the Kwanjeong scholarship. (Corresponding author: Michael A. Lin.)

M. A. Lin, A. F. Siu, J. H. Bae, and M. R. Cutkosky are with the Department of Mechanical Engineering, Stanford University, Stanford, CA 94305 USA (e-mail: mlinyang@stanford.edu; afsiu@stanford.edu; jbae7@stanford.edu; cutkosky@stanford.edu).

B. L. Daniel is with the Department of Radiology, Stanford University, Stanford, CA 94305 USA (e-mail: bdaniel@stanford.edu).

This letter has supplementary downloadable material available at <http://ieeexplore.ieee.org>, provided by the authors. The Supplemental Materials include a video showing the first-person view of the HoloNeedle guidance system displaying a 2-mm target embedded in phantom tissue and a virtual medical needle showing the position and shape of a real medical needle. This material is 7.95 MB in size.

Digital Object Identifier 10.1109/LRA.2018.2863381

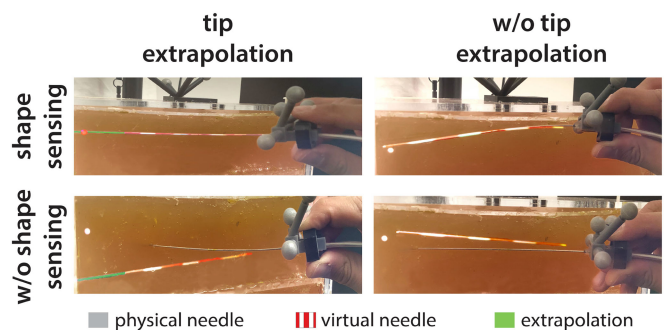
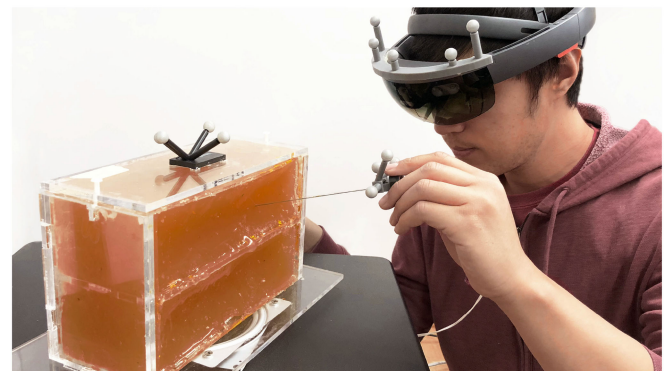


Fig. 1. Needle placement experiment setup. *Top*: A HoloLens AR display is used to visualize position and shape of needle as inserted into phantom tissue. *Bottom*: First person view of the needle and targets under four condition which include combinations of shape sensing and TTE.

(i) physicians must recover 3D information (e.g. depth of structures) from 2D images, (ii) needles may introduce artifacts in the images that make it challenging to identify the tip and target [1], [2], (iii) they require complex hand-eye coordination for registering the images seen in an external monitor to the patient's anatomy [3]. Thus significant practice is needed to overcome a steep learning curve [4].

Several works have explored the use of mixed- or augmented-reality in medical applications (e.g., laparoscopy [3], breast resection [5], maxillofacial surgery [6], [7]), with the goal of restoring the physician's natural point of view and head motion parallax necessary for understanding 3D structures. In needle biopsy guidance, Fuchs *et al.* pioneered the use of AR to display real-time US images directly on the patient such that the physician can visualize the needle as it is inserted [8]. US, however, is only capable of displaying one image plane at a time

and thus requires careful alignment of the needle to the imaging probe Rosenthal *et al.* solved this problem by tracking the needle and displaying it virtually so that US was only critical for visualizing the surrounding areas [9]. Sauer *et al.* showed augmentation was intuitive enough that users without prior medical training could consistently place a needle within 6 mm [10]. In practice, these methods suffer from the assumption of the needle being modeled and displayed as a rigid shaft. Upon insertion, deflections occur producing errors that are amplified as needle is inserted further into tissue [11]. These deflections can lead to errors in needle placement of 4 mm up to 12 mm [12], [13]. Sensing and updating the shape of the needle in rendering can be essential for achieving precision and bringing these methods closer to a clinical setting.

In this work we investigate the benefits of displaying shape sensing information in a needle biopsy guidance system and in what ways this information can be displayed through AR to increase placement accuracy without requiring extensive training. To enable this work, we introduce HoloNeedle, an AR-guided needle biopsy system. The system uses optical shape sensing, derived from [14] and augments it with optical marker tracking at the needle base. The result provides fast, accurate 3D reconstruction of needle position, orientation and deflection for use with a head-mounted AR display (Microsoft HoloLens).

The HoloNeedle system addresses several of the issues discussed previously for traditional needle guidance methods. This system displays the needle and medical images containing the targets registered to their physical counterparts. This allows the user to know where the needle is inside the tissue and how their hand movement affects the needle tip. It also allows the user to perform the task while looking at the patient which reduces hand-eye coordination complexity. Moreover, with the AR headset, additional cues can be provided to the user. We demonstrate adding a virtual extension of the needle tip to give users a better understanding of what path the needle will take.

To demonstrate the advantages of accurately displaying the needle shape and location and restoring users' natural perspective, we conducted a controlled study where novice users were tasked to place a medical needle in a 2 mm target within a phantom tissue under three conditions: (i) displaying the needle as a rigid shaft, (ii) displaying the needle with real-time shape updated, and (iii) displaying needle with a virtual ray extending tangentially out of the tip (TTE) in addition to the needle's position, orientation and shape (Fig. 1). We refer to the TTE feature in combination with shape-sensing as STTE. Results show a 20% and 26% decrease in norm error in the shape-sensing and STTE conditions, respectively, when compared to the rigid condition. Moreover, participants self-reported a 14% and 53% increase in perceived performance in the shape-sensing condition and STTE conditions, respectively, compared to the rigid condition.

## II. SYSTEM DESIGN

The needle placement guidance system consists of three major components: (i) a head-mounted stereoscopic AR display (Microsoft HoloLens V1), (ii) a medical needle embedded with

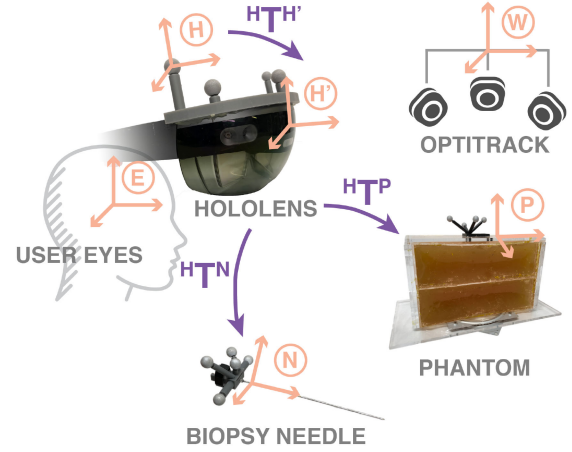


Fig. 2. Reference frames of HoloNeedle components. H, P and N correspond to reference frames defined by OptiTrack markers on the HoloLens, Phantom, and Needle. These are used to find the relative transforms  ${}^H T^P$  and  ${}^H T^N$  for displaying virtual targets and needle, respectively.

strain sensors and (iii) a commercial motion tracking system (OptiTrack Flex 13). The HoloLens is a stand-alone AR device with its own core processing unit that can display 3D objects embedded in the user's surroundings.

### A. Rigid Object Tracking

In order to render the position of the virtual needle, a real-time high precision tracking method of the needle base is needed. Although the HoloLens is equipped with depth and time-of-flight IR cameras capable tracking objects in 3D, these sensors have a limited sampling rate of around 5 Hz, which is not good enough for tracking moving objects. An alternative option is to track the needle using the built-in RGB camera on the HoloLens and computer vision algorithms such as Vuforia SDK [15] to extract pose information of the needle based through attached track visual markers (printed 2D patterns); however, the accuracy of this tracking method is too limited for this application. In particular, since we are tracking the needle base, small rotation errors result in a substantial error in the display of the needle tip position. To render the guidance holograms well aligned to their physical counterparts, an OptiTrack Flex 13 motion tracking system is used to obtain high accuracy (approx. 0.05 mm RMS) pose information of the needle handle and the tissue target relative to the head-mounted display. The tracking cameras were anchored to the room and set up for a 1 m<sup>3</sup> table-top workspace which was enough to allow the users to freely move without losing tracking of the objects. Fig. 1 shows the HoloLens, the needle and phantom tissue container instrumented with custom made infrared reflective markers that can be tracked by the OptiTrack. The tracking software defines an arbitrary reference frame for each marker denoted in Fig. 2 as H, N and P, respectively.

OptiTrack provides tracking info as  ${}^W T^H$ ,  ${}^W T^N$  and  ${}^W T^P$ , where each of these is a 4x4 matrix transform from room-fixed reference frame (W) to each of the rigid body markers. To render the needle and the tissue targets, the HoloLens needs  ${}^{H'} T^N$  and  ${}^{H'} T^P$  (shown in Fig. 2), respectively. Where  $H'$  indicates the reference frame of the HoloLens relative to which holograms

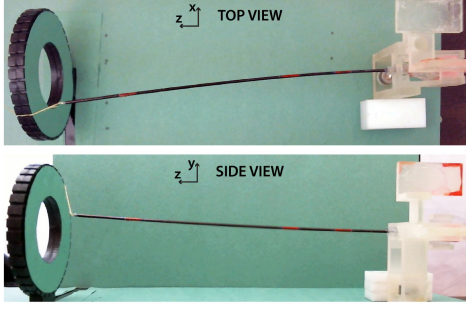


Fig. 3. Needle calibration setup using two cameras from top view (Top) and side view (Bottom).

are rendered. These two transformations can be calculated as:

$$\begin{aligned} H'T^N &= H'T^H \cdot H'T^W \cdot W'T^N \\ H'T^P &= H'T^H \cdot H'T^W \cdot W'T^P \end{aligned} \quad (1)$$

A one-time calibration process is needed to find  $H'T^H$ . The HoloLens provides a pre-calibrated transformation  $H'T^C$  where C is the reference frame of the built-in RGB camera. Using Vuforia SDK, we are able to get the pose of a visual marker relative to the C reference frame. We attached a Vuforia visual marker (A) to a OptiTrack marker (B) such that their reference frames matched exactly (i.e.  $A'T^B = I$ ). Then knowing that  $A'T^B = I$ , we calculated  $H'T^H = H'T^A \cdot A'T^B \cdot B'T^H = H'T^A \cdot B'T^H$ . The final calibration result was obtained by taking the average of multiple samples of  $H'T^H$  in order to reduce the error from the visual marker tracking.

### B. Needle Shape Sensing

The rigid body tracking method allowed us to accurately determine the location of the needle base in real-time. Using this point as origin, the rest of the needle shape is rendered based on measurements from embedded FBG sensors. FBGs are optical strain gauges that are highly sensitive to mechanical strain. They are a popular choice for sensing needle shape because of their thin form factor (typically 85–125  $\mu\text{m}$  diameter) which makes them suitable for embedding within the stylet of a needle.

The shape sensing needle is a 145 mm long, 18 G symmetric tip needle instrumented with three triplets of FBG sensors located at 31 mm, 81 mm and 131 mm from the base. Sensor locations were chosen based on a combination of Monte Carlo simulation results to maximize sensor signal, subject to manufacturing constraints [14], [16]. A SM130 (2 kHz sampling rate) Micron Optics interrogator was used to sample the strain sensors at 100 Hz.

1) *Calibration*: Calibration of the needle was performed with two digital cameras capturing the shape of the needle from two orthogonal views while changing the amount of deflection as shown in Fig. 3. Changes in wavelengths were sampled from the sensors, and curvature at the sensor location was obtained from fitting a center line to the images taken from the two digital cameras. The needle was loaded at the tip in 14 different configurations such that 7 deflections were mostly on the XZ plane and 7 deflections were on the YZ plane. Calibration produced

three calibration matrices for the three sensor triplets along the needle.

2) *Reconstruction*: Each matrix maps strain readings to a needle curvature in the XZ and YZ plane. We approximate the needle bending as the result of a tip load. Using Euler-Bernoulli beam theory a linear model fits the rest of the curvature along the needle. During a needle insertion, the loading on the needle is more complicated as it depends on the amount of needle already inserted in tissue. But as noted [14] the high stiffness of the needle compared to tissue acts as a low-pass filter to high spatial frequency loading along the needle. For this reason, the deflection of the needle can be approximated as a tip load. This model can be improved if additional sensors are used to obtain the amount of needle inserted in tissue but we leave this for future improvements.

The calibrated sensor readings only inform us on the curvature along the needle projected in XZ and YZ planes. In order to obtain the 3D deflection of the needle based on these projected curvatures, we approximated the needle as a chain of short constant-length links. Based on the definition of curvature  $K = d\theta/ds$ , 2D rotation of each link with respect to the previous proximal link is  $\theta = l \cdot \overline{K}_i$ , where  $l$  is the length of each link and  $\overline{K}_i$  is the mean curvature of the needle along this segment in a plane. It is straightforward to obtain the deflection of the needle in the projected XZ and YZ planes from the curvature in each plane ( $K_x$  and  $K_y$ , respectively). However, these two projected deflections need to be combined into one 3D deflection. Let  $\theta_i$  be the rotation of a link  $i$  relative to link  $i - 1$  and  $\hat{r}$  be the projected needle length in YZ plane, and  $\phi_i$  be the rotation and  $\bar{r}$  be the projected needle length in XZ plane. Then we have:

$$\begin{aligned} x_i &= \bar{r} \sin \phi_i, & z_i &= \bar{r} \cos \phi_i \\ y_i &= \hat{r} \sin \theta_i, & z_i &= \hat{r} \cos \theta_i \end{aligned} \quad (2)$$

$$\bar{r} \cos \phi_i = \hat{r} \cos \theta_i \quad (3)$$

where  $\theta_i = \theta_{i-1} + l \cdot \overline{K}_{yi}$  and  $\phi_i = \phi_{i-1} + l \cdot \overline{K}_{xi}$ .

We are interested in finding the coordinate  $(x_i, y_i, z_i)$ , which is the distal end of each link.

$$l^2 = x^2 + y^2 + z^2 \quad (4)$$

$$= \bar{r}^2 \sin^2 \phi_i + \hat{r}^2 \sin^2 \theta_i + \bar{r}^2 \cos^2 \phi_i \quad (5)$$

$$\bar{r} = \sqrt{\frac{l^2}{\sin^2 \phi_i + \left(\frac{\cos \phi_i}{\cos \theta_i}\right)^2 \sin^2 \theta_i + \cos^2 \phi_i}} = \alpha \quad (6)$$

Finally, we substitute  $\bar{r}$  into (2) to get

$$x_i = \alpha \sin \phi_i \quad (7)$$

$$y_i = \alpha \tan \theta_i \cos \phi_i \quad (8)$$

$$z_i = \alpha \cos \phi_i \quad (9)$$

With equations (7)–(9), it is possible to find the approximated 3D reconstruction of the entire needle deflection.

Results from the calibration and reconstruction method are shown in Fig. 4. The plot shows the reconstructed needle shape (in red) and the shape of the needle obtained from the camera



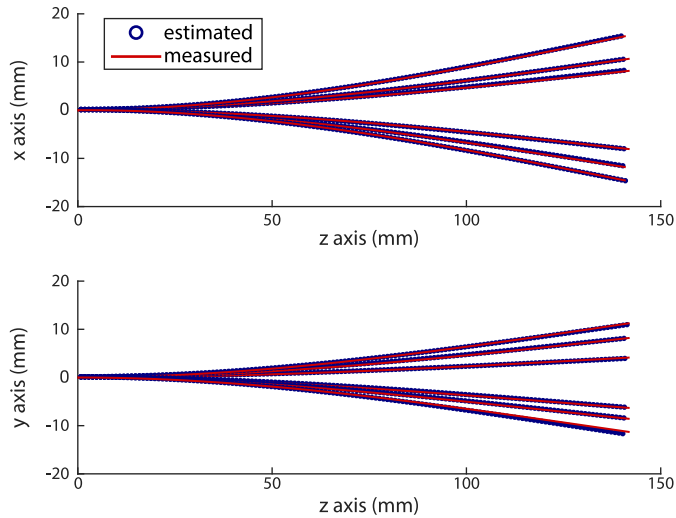


Fig. 4. Results of needle calibration. Reconstructed needle shape is shown in blue and measured needle shape from camera is shown in red.

(in blue). The mean norm error of the tip estimate in the XZ plane was 1.30 mm, and in the YZ plane was 1.54 mm.

### C. Additional Assisting Graphics

A problem observed during initial pilot tests was that users had difficulty determining whether the needle was aligned to a target located far from the tip. Alignment only became clear when the needle was inserted near the target, but usually by then, it was difficult to correct the needle path. To assist the user in these scenarios, the system was also programmed to project a ray from the needle tip to help the user extrapolate the direction of the tip as illustrated in Fig. 1.

## III. EVALUATION IN A NEEDLE PLACEMENT TASK

### A. Materials & Setup

An IRB-approved user experiment (IRB-26526) was performed to evaluate the system. The experiment consisted of a needle insertion task assisted by three different augmentation strategies. The insertion task was performed on an opaque phantom tissue inside which virtual targets were placed.

Phantom tissue was made from M-F Manufacturing polyvinyl chloride-plastisol (PVCPl) with a mixture of 4:1 plastic to softener. The phantom tissue container was of size  $25.4 \times 14.5 \times 10.5$  cm, designed such that multiple insertions could be performed on one phantom. Moreover, the phantom was mounted on a rotating platform so users would be able to look at the targets from different perspectives and have more clear depth cues of the holograms by taking advantage of motion parallax. In practice, when using an AR system, users receive these depth cues mostly through head motion parallax. In the case of this experiment, it was simpler to make the phantom tissue rotating rather than building a setup where users could walk around the phantom.

The displayed virtual targets were small white spheres of 2 mm diameter. Their position was defined relative to the origin of the phantom reference frame (P in Fig. 2). The targets were displayed at either 3 cm (shallow) or 7 cm (deep) away from

the insertion surface. These two depths were chosen to simulate shallow and deep lesion locations, where deep lesions have been reported to result in higher placement errors than shallow lesions [11].

There were three conditions under which participants performed the task:

- 1) Rigid condition (R): virtual needle tracks the physical needle in position and rotation but not in shape.
- 2) Shape sensing condition (S): virtual needle tracks the physical needle in position, rotation and shape.
- 3) Shape Sensing + TTE condition (STTE): virtual needle tracks the physical needle in position, rotation and shape. Additionally, a ray is projected tangentially out of the tip of the needle and the target temporarily changes to red color when the ray intersects with it.

The condition using TTE without shape sensing was not included in the experiment because the lack of shape sensing caused the extrapolated ray to appear very off from the actual tip direction as can be seen in Fig. 1.

### B. Experiment Procedure

Before the experiment, depth rendering was calibrated for each user to ensure proper registration of virtual to physical objects. Users followed instructions from a built-in HoloLens calibration software to perform a task-based Inter-Pupillary Distance (IPD) measurement. This one-time IPD measurement was used for the rest of the experiment.

Users were also asked to perform a headset alignment task in which they were presented with a cube with OptiTrack markers and a virtual cube of equal dimensions overlaid. Users would manually adjust the position of the HoloLens (left, right, up and down) until the hologram aligned to its physical counterpart. Headset misalignments are a well-known problem in the mixed/augmented reality field [17] and occur when users wear the head-mounted display such that their eyes are at an off-set position from their assumed positions as pre-programmed in the HoloLens. This causes holograms to appear offset from where they are meant to be displayed. This alignment task was performed each time the user wore the head-mounted display.

The experiment began with a practice session where users performed 12 insertions with 4 insertions per condition. They were instructed to insert the needle with the primary goal of placing the tip of the virtual needle as close as possible to the center of the displayed target without any time constraints. They were encouraged to rotate the phantom to look at the virtual target and needle from different angles such that depth perception was not disadvantaged in any preferred direction. Training lasted approximately 15 minutes.

Training was followed by three experiment sessions with a total of 36 insertions per user (12 insertions for each condition). Each session comprised a different condition; order was counterbalanced following a Latin Squares design. For each insertion, one target of unique location was displayed at a time and target locations were presented in a randomized order to minimize memorization of previous target locations. Target depth in each condition was distributed as half shallow and half deep.

After each session, users completed a survey with questions regarding the condition they had just performed and then took a 5-minute break. The entire experiment lasted on average one hour and 15 minutes.

### C. Data Collection

Needle placement errors between the final needle tip position and the virtual target position were measured as 3D vectors. Norms of these error vectors were used for statistical analysis. To track the needle tip final position, short needle cannula tips were custom made to be worn during each insertion. These tips were made of thin flexible polyvinyl tubing (1.5 mm inner diam, 0.5 mm wall thickness) capped on one end with a 1.5 mm acrylic bead. During each insertion tips were pushed in as the needle was inserted and stayed in the phantom when the needle was retracted. Users were trained to insert the needle with these tips making sure to never retract the needle unless they were done with the insertion.

The position of these tips in the phantom tissue was measured after each experiment by taking a 3D scan of the phantom tissue using a volumetric cone-beam CT scanner (Artis Zeego, Siemens Medical, Erlangen, Germany). Only the acrylic bead of the tip showed good contrast in the images, thus their centroid was used to determine the tip position. These positions were measured in reference frame P (Fig. 2) so that they could be compared to the target locations.

In addition to the needle placement accuracy, FBG sensor data and OptiTrack marker tracking data were also recorded. Qualitative data obtained from surveys after each session contained questions based on the NASA Task Load Index (TLX) questionnaire and questions rating the users confidence in reaching the target at different insertion stages.

### D. Participants

A total of 12 users (3 female, mean age 28) participated in the experiment. Three users reported to have previous experience with AR devices and only one user reported previous experience with medical needles.

### E. Hypothesis

Needle deflections that occur during an insertion procedure are significant such that they lead to errors in the accuracy of needle placement. Thus, we hypothesize that needle placements performed in condition S will have a significantly lower placement error compared to needle placements performed in the condition R (H1). In addition, STTE augmentation provides the users with more clear visual feedback of the needle and target alignment before and during needle insertion and thus will result in lowest placement error (H2).

### F. Results

*Needle placement mean norm error for shallow (3 cm) and deep (7 cm) targets.* The needle placement error was compared between deep (D) and shallow (S) targets. The difference between D and S was normally distributed (assessed by a

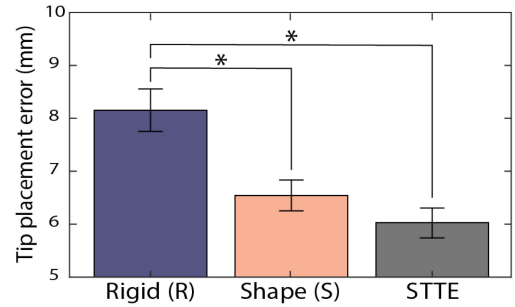


Fig. 5. Needle placement accuracy for each condition. Results for each condition were rigid (R):  $\mu = 8.15$ ,  $SE = 0.4$ , shape (S):  $\mu = 6.54$ ,  $SE = 0.294$  and STTE:  $\mu = 6.03$ ,  $SE = 0.291$ .

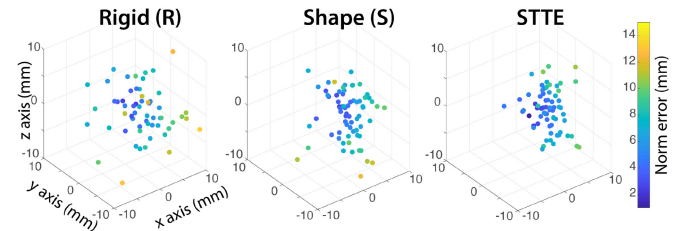


Fig. 6. 3D scatter plot shows spread of needle placement error in each condition. Coordinate axis correspond to ref. frame P shown in Fig. 2.

Shapiro-Wilks test,  $p > 0.6$ ). A two-tailed paired t-test revealed significant differences from depth on needle placement mean error ( $t(219) = 5.64$ ,  $p = 5.6e - 08$ ). Mean norm error for shallow targets was  $\mu = 5.67$  mm (Std. Err. (SE)= 0.15) and deep targets was  $\mu = 7.08$  mm ( $SE = 0.2$ ).

*Needle placement mean norm error between conditions.* The norm error data for each condition did not satisfy the Shapiro-Wilks test. A Friedman test comparing mean norm error between conditions at 3 cm depth revealed no significant effect of the condition on needle placement error. Another Friedman test on data points from targets at 7 cm revealed a significant effect of the condition on placement error ( $\chi^2(1) = 17.1$ ,  $p < 1.9774e - 04$ ). A post-hoc pairwise comparison with Bonferroni correction showed significant difference between conditions R and S ( $p < 0.0029$ ) and between conditions R and STTE ( $p < 0.0004$ ). Fig. 5 shows the error results from conditions R ( $\mu = 8.15$  mm,  $SE = 0.4$ ), S ( $\mu = 6.54$  mm,  $SE = 0.294$ ) and STTE ( $\mu = 6.03$  mm,  $SE = 0.291$ ). Fig. 6 shows 3D scatter plots of placement error for targets at 7 cm in each of the conditions. On average, there was a 20% and 26% decrease in norm error in the S and STTE conditions, respectively, when compared to the R condition.

*Needle placement time.* The mean time (in seconds) to complete the needle insertion for each condition was R:  $\mu = 30.5$ ,  $SE = 1.65$ , S:  $\mu = 26.28$ ,  $SE = 2.07$  and STTE:  $\mu = 29.72$ ,  $SE = 1.92$ . A Friedman test revealed no significant effects of conditions on completion time.

*NASA TLX.* Fig. 7 summarizes results from the TLX questionnaire. Friedman tests revealed significant differences in frustration ( $\chi^2(2) = 8.7$ ,  $p < 0.013$ ). A post-hoc pairwise comparison with Bonferroni correction showed significant difference between conditions R and STTE ( $p = 0.013$ ). Tests

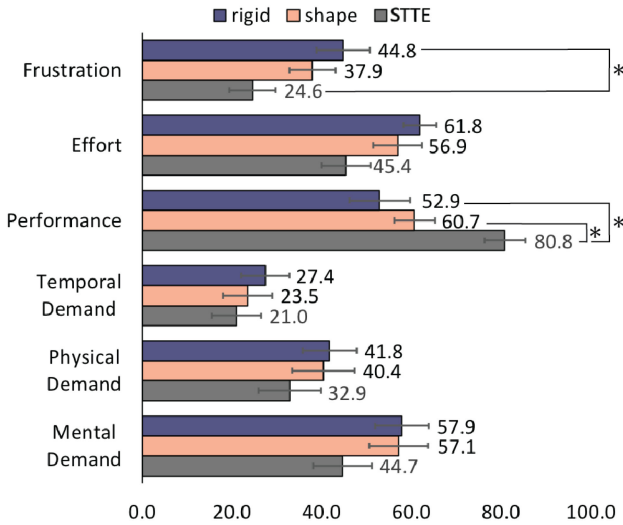


Fig. 7. Self-reported mean task load ratings for all three conditions ( $N=12$ ). Mean perceived performance increased by 14% for S condition compared to R condition. Mean perceived performance increased by 53% and frustration decreased by 45% for STTE condition compared to R condition.

also revealed significant differences in perceived performance ( $\chi^2(2) = 11.9, p < 0.0026$ ). A post-hoc pairwise comparison with Bonferroni correction showed significant difference between conditions R and S ( $p = 0.015$ ), and conditions R and STTE ( $p = 0.0053$ ). Perceived performance increased by 14% for condition S compared to R. Perceived performance increased by 53% and frustration decreased by 45% for STTE condition compared to R.

**Qualitative feedback.** Users described that their strategy in the STTE condition was to use the ray to align the needle to the target as well as possible before starting the insertion. This allowed them to be confident in the needle alignment, “The targeting feature erased all of my doubts about physical and virtual needle alignment.” They also used the ray as an indicator of how far the tip was from the target, so motion parallax was less critical. In contrast, users described that their strategy in the R condition was to insert the needle first and adjust when closer to the target by turning to a side view. Some users described this condition as “...the most challenging and the most frustrating task...”

#### IV. DISCUSSION

Similar to previous works, we found that placement errors increase for targets that are deeper in the tissue [11]. A possible reason for this is that any early misalignments are amplified the deeper the needle is inserted since it becomes harder to steer the needle when more tissue holds onto the needle shaft.

Needle placement errors for shallow targets were similar among all conditions. This may be because it was easier to align the needle to shallow targets before starting insertion. Moreover, since the travel path is shorter there is less chance for deflections to affect placement. Thus providing the additional information given in conditions S and STTE may be less beneficial for this depth of target.

In the case of deep targets, results show that displaying the needle shape and TTE are beneficial to reducing placement

errors (H1). This result is observable in Fig. 6. Needle placements for deep targets had a larger error spread in all directions for condition R compared to the other two conditions. Lower needle placement error in both conditions that included shape sensing (S and STTE) indicate that users are able to use the shape information to perform needle placements with significantly more accuracy.

STTE resulted in the lowest placement error (H2), but perhaps the most noticeable benefit of this form of augmentation is the reduced amount of frustration (−53%) and increased amount of perceived performance (+45%) as self-reported by users. Various users noted that TTE information allowed them to continuously verify alignment of the needle to the target and make corrections early. This may not only lead to lower placement errors but also prevent cutting through a lot of tissue caused by steering. Another advantage, is that the extrapolation ray serves as an indicator of the distance between the tip and the target. Thus, users noted that, with TTE, they did not need to constantly look at the needle and target from different viewing angles to gain more visual depth cues as it was the case in conditions R and S.

#### V. LIMITATIONS AND FUTURE WORK

An important assumption in the needle guidance system was that the targets in tissue are rigidly attached to the tracking marker, but in practice the position of these targets may shift since tissue is deformable. One possible way to avoid this assumption is to complement the system with a real-time imaging method, such as US, for visualizing the target plane. Imaging would be dedicated to updating the position of targets while AR is used for navigation guidance.

Another way to increase the system accuracy is to improve the model of the needle curvature. The current linear model assumption may lead to errors in practice due to additional concentrated loading from the patient skin. A piece-wise linear model may be able to yield a more accurate shape reconstruction, at the cost of requiring an additional sensor to detect the amount of needle insertion. Alternatively, shape reconstruction accuracy can be also improved by using more complex models [18].

Furthermore, there could be other augmentation strategies that could help improve placement accuracy. For example, knowing the target location and incorporating surgical pre-planning data, the system could suggest optimal insertion points to reach the target. Augmentation can also be used to provide more explicit directional cues and/or warnings when users are off path.

In this study we only recruited non-medical users, but it would be interesting to include experienced medical users in future studies as this may further inform on improvements to the AR system that could increase needle placement accuracy.

#### VI. CONCLUSION

We have shown that sensing and displaying the shape of the needle in an AR-guided needle biopsy system, such as HoloNeedle, can significantly increase needle placement accuracy even for non-medical users without prior training. We also demonstrated how augmented-reality can be used to provide users with

additional guidance cues throughout the procedure. For example, we extrapolated the heading of the needle tip and showed that this representation decreased users' self-reported frustration and increased perceived performance. These augmentation strategies allowed users with non-medical training to achieve low error rates.

While results presented here are preliminary, they validate important design guidelines for future implementations of AR guidance systems for flexible medical tools. As the field of AR continues to grow and displays become more inexpensive and practical, we hope further research can bring this type of guidance system closer to clinical practice.

#### ACKNOWLEDGMENT

The authors would like to thank S. Bonaretti and R. Bennett for help using the CT scanner, and S. Perkins and C. Leuze for their valuable insights.

#### REFERENCES

- [1] W. Xia *et al.*, "In-plane ultrasonic needle tracking using a fiber-optic hydrophone," *Med. Phys.*, vol. 42, no. 10, pp. 5983–5991, 2015.
- [2] M.-C. Chevrier, J. David, M. El Khoury, L. Lalonde, M. Labelle, and I. Trop, "Breast biopsies under magnetic resonance imaging guidance: Challenges of an essential but imperfect technique," *Current Problems Diagnostic Radiol.*, vol. 45, no. 3, pp. 193–204, 2016.
- [3] H. Fuchs *et al.*, "Augmented reality visualization for laparoscopic surgery," in *Proc. Med. Image Comput. Comput.-Assisted Intervention*, 1998, pp. 934–943.
- [4] S. Adhikary, A. Hadzic, and P. McQuillan, "Simulator for teaching hand-eye coordination during ultrasound-guided regional anaesthesia," *Brit. J. Anaesthesia*, vol. 111, no. 5, pp. 844–845, 2013.
- [5] Y. Sato *et al.*, "Image guidance of breast cancer surgery using 3-d ultrasound images and augmented reality visualization," *IEEE Trans. Med. Imag.*, vol. 17, no. 5, pp. 681–693, Oct. 1998.
- [6] M. Zhu *et al.*, "A novel augmented reality system for displaying inferior alveolar nerve bundles in maxillofacial surgery," *Sci. Rep.*, vol. 7, 2017, Art. no. 42365.
- [7] M. Qu *et al.*, "Precise positioning of an intraoral distractor using augmented reality in patients with hemifacial microsomia," *J. Cranio-Maxillo-Facial Surg.*, vol. 43, no. 1, pp. 106–112, 2015.
- [8] H. Fuchs *et al.*, "Towards performing ultrasound-guided needle biopsies from within a head-mounted display," in *Visualization in Biomedical Computing*. Berlin, Germany: Springer, 1996, pp. 591–600.
- [9] M. Rosenthal *et al.*, "Augmented reality guidance for needle biopsies: An initial randomized, controlled trial in phantoms," *Med. Image Anal.*, vol. 6, no. 3, pp. 313–320, 2002.
- [10] F. Sauer, A. Khamene, and S. Vogt, "An augmented reality navigation system with a single-camera tracker: System design and needle biopsy phantom trial," in *Proc. Med. Image Comput. Comput.-Assisted Intervention*, 2002, pp. 116–124.
- [11] M. Z. Papa *et al.*, "The effect of anesthesia type on needle localization breast biopsy: Another point of view," *Amer. J. Surg.*, vol. 171, no. 2, pp. 242–243, 1996.
- [12] A. Khamene *et al.*, "An augmented reality system for MRI-guided needle biopsies," *Stud. Health Technol. Inform.*, vol. 94, pp. 151–157, 2003.
- [13] P. Blumenfeld *et al.*, "Transperineal prostate biopsy under magnetic resonance image guidance: A needle placement accuracy study," *J. Magn. Reson. Imag.*, vol. 26, no. 3, pp. 688–694, 2007.
- [14] Y.-L. Park *et al.*, "Real-time estimation of 3-d needle shape and deflection for MRI-guided interventions," *IEEE/ASME Trans. Mechatron.*, vol. 15, no. 6, pp. 906–915, Dec. 2010.
- [15] "Vuforia augmented reality SDK." [Online]. Available: [www.vuforia.com](http://www.vuforia.com), Accessed on Aug. 7, 2018.
- [16] S. Elayaperumal *et al.*, "MR-compatible biopsy needle with enhanced tip force sensing," in *Proc. World Haptics Conf.*, 2013, pp. 109–114.
- [17] R. Azuma and G. Bishop, "Improving static and dynamic registration in an optical see-through HMD," in *Proc. SIGGRAPH*, 1994, pp. 197–204.
- [18] R. J. Roesthuis, M. Kemp, J. J. van den Dobbelsteen, and S. Misra, "Three-dimensional needle shape reconstruction using an array of fiber bragg grating sensors," *IEEE/ASME Trans. Mechatron.*, vol. 19, no. 4, pp. 1115–1126, Aug. 2014.